Structural and chemical changes from CO_2 exposure to self-healing polymer cement composites for geothermal wellbores

Mohamed S. Elbakhshwan[a], Simerjeet K. Gill[b,*], Kenton A. Rod[c], Emma B. Bingham[d], Adriana L. McKinney[d], Nicolas Huerta[c], Christina L. Lopano[e], Barbara G. Kutchko[e], Yu-chen Karen Chen-Wiegart[f,g], Chonghang Zhao[f], Garth Williams[g], Juergen Thieme[g], Tamas Varga[d], Lynne E. Ecker[b], Carlos A. Fernandez[c,*]

[a] Engineering Physics Department, University of Wisconsin Madison, United States
[b] Nuclear Science and Technology Department, Brookhaven National Laboratory, United States
[c] Energy and Environment Directorate, Pacific Northwestern National Laboratory, United States
[d] Environmental and Molecular Sciences Laboratory, Pacific Northwest National Laboratory, United States
[e] Research and Innovation Center, National Energy Technology Laboratory, United States
[f] Material Science and Chemical Engineering Department, Stony Brook University, United States
[g] National Synchrotron Light Source II, Brookhaven National Laboratory, United States

ARTICLE INFO

ABSTRACT

Wellbore cement is subjected to a number of mechanical, thermal and chemical stress regimes over its lifetime. Therefore, next-generation wellbore cement formulations need to be evaluated in conditions relevant to these environments. In this work, we investigate the mechanism of the alteration of a novel self-healing polymer-cement composite after exposure to a CO_2-rich environment by using synchrotron-based X-ray Fluorescence (XRF), X-ray absorption near edge structure (XANES), and scanning electron microscopy coupled with energy dispersive spectroscopy. Results showed that a chemical alteration of the polymer-cement follows the rim carbonation mechanism, similar to conventional cement, although carbonation takes place to a lesser extent in polymer-cements despite the higher porosity. Along with detailed mechanistic insights on carbonation in polymer-cement composite, the performance of these in CO_2-rich environment is further studied using standard compressive strength analysis.

1. Introduction

In an increasingly energy-demanding world, geothermal energy promises to become a sustainable and large-scale source of energy in the United States and around the globe. However, the extreme conditions at which energy recovery operations take place, particularly in Enhanced Geothermal Systems (EGS), limits dramatically their contribution as a major energy source (Bachu, 2000; Zhang and Bachu, 2011; Nelson et al., 2006; Shortall et al., 2015). During drilling, stimulation, and later, wellbore completion and geothermal plant operations, it is critical for the wellbore casing and cement (the hydraulically insulating layer between casing and formation) to maintain their integrity. This is because if damaged they can introduce engineered-leakage pathways linking the geological reservoirs with drilling, stimulation, or working fluids. In the specific case of wellbore cement, it is the inherent reactivity inside geothermal wellbores, such as acidic CO_2 rich fluids in the reservoir, alkalinity of cements and corrosion of steel casing, that make wellbores vulnerable to high-risk leakage pathways (Carroll et al., 2017; Kutchko et al., 2009a; Carey, 2013; Um et al., 2014a; Jung et al., 2014; Um et al., 2014b). Sealing failure of the cement lining as a result of mechanical, thermal, and chemical stress is a usual problem that introduces massive consequences, including environmental contamination, and very expensive major repair operations with the additional loss of millions of dollars due to production stoppage. Therefore, there is a need for advanced cement technologies with the potential to reduce the probability of cracking and cement-steel casing and cement-formation rock debonding.

To ensure the long-term integrity of the wellbore and minimize risk of leakage, we recently developed a novel self-healing cement by adding a self-healable thermoset epoxy resin (glass transition temperature, T_g = -33 °C and a thermal stability of up to 260 °C) to well cement (Ian Childers et al., 2017). It was shown that on fractured
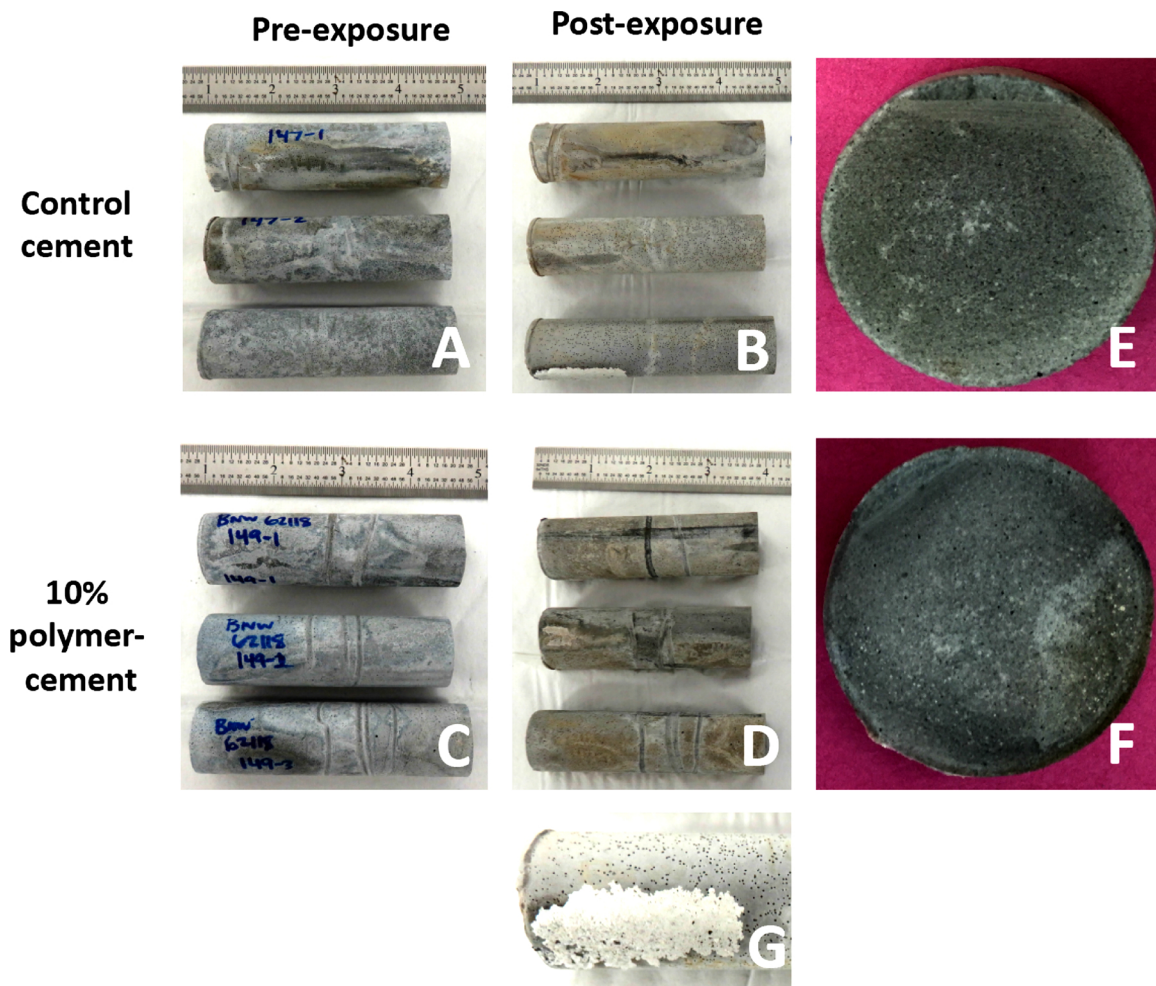
Fig. 1. Pictures of the control and composite cements taken before (A, B) and after (C-F) exposure to brine−CO$_2$ environment. White precipitate was observed on both control and polymer cement samples after exposure to CO$_2$, but the precipitate was significantly more dominant on control cement samples (see bottom picture G, which is the magnified version of bottom most sample in B).

surfaces, the polymer strongly anchors through ionic Ca−O bonds resulting from the deprotonation of polymer hydroxyl groups while the polymer S−S groups are turned away from the cement−polymer interface, allowing for the self-healing function within the polymer (Nguyen et al., 2018). The novel cementitious material was demonstrated to seal fractures with 0.3−0.5 mm apertures, two orders of magnitude larger than typical wellbore fractures with permeability reductions of up to 87 % on tensile fractures (Fig. 1) (Ian Childers et al., 2017). Self-healing cements offer the capability of autonomous fracture repair, reducing the need for stopping operation to remove the damaged cement and pumping new cement with the associated cost savings.

Naturally occurring CO$_2$ as well as CO$_2$-enriched working fluids are present before and during geothermal plant operations. During geothermal plant operations, non-condensable gases are carried by the geofluid and are released during condensation prior to reinjection. Typically, CO$_2$ makes up over 90 % of non-condensable gases, with the rest being shared by primarily hydrogen sulfide and other gases, such as hydrogen and methane (Paulillo et al., 2019; Milestone et al., 2010). Similarly, mineral acids (typically hydrochloric or sulfuric acid) are used as part of stimulation operations to increase formation rock permeability. This is particularly the case for tight oil stimulation operations (Malate et al., 1998; Lucas et al., 2020). Therefore, given the mechanical, thermal (up to 400 °C), and chemical stress regimes of the wellbore environment, it is important to test the cement's performance in various simulated downhole conditions to determine their overall

integrity (Nelson et al., 2006; Barlet-Gouédard et al., 2007; Barlet-Gouédard et al., 2009). The objective of this work is to understand the elemental, structural and chemical changes that these self-healing polymer-cement composites undergo after exposure to CO$_2$ environments using high-resolution synchrotron methods to assess their potential for application in geothermal wellbores. X-ray fluorescence (XRF) was used to identify and map out the elemental changes at the cement−CO$_2$ interface after exposure. Micro X-ray absorption near edge structure (XANES) was used to identify the chemical structure of the carbonation products formed. In addition, the changes in surface (cement−CO$_2$ interface) and internal structure after exposure to CO$_2$ was investigated using scanning electron microscopy (SEM) coupled with energy dispersive spectroscopy (EDS) and micro-tomography. Compressive strength was measured to correlate the chemical alteration with the overall structural integrity of the cement. Findings from our work establishes a fundamental understanding of the changes in both microstructure and chemical structure of the self-healing polymer-cement composites after CO$_2$-cement interactions.

2. Materials and methods

2.1. Sample preparation

The polymer was prepared by mixing the monomers epoxidized polysulfides Thioplast EPS25 (8.4 g, herein EPS25), poly(ethylene glycol) diglycidyl ether (8.4 g, herein PEO), and pentaerythritol tetrakis

(3-mercaptopropionate) (5.7 g, herein 4SH) in an Al pan. Samples of conventional wellbore cement were prepared by mixing class H cement powder (157.5 g), silica flour (67.5 g), and DI water (85.5 g for control and 112.5 g for cement-polymer composite) in a poly(propylene) beaker to form a cement slurry. The water-to-cement ratio and cement-to-silica flour ratio was 0.58 and 7:3, respectively. The cement was transferred to plastic molds and placed in a container surrounded by water and covered with aluminum foil, then cured at a temperature of 85 °C for 24 h. Polymer-cement composites were created by adding the monomers mixture to the cement slurry (prepared with the above described water-to-cement and cement-to-silica flour ratios) and mixed to give polymer-cement slurries and then cured in a high humidity environment at 85 °C for 24 h as previously reported (Ian Childers et al., 2017). The polymer concentration in the cement (9 wt%) was chosen based on our previous study where it was shown that compressive strength after 24 h and 7 days is one of the highest for this polymer-cement composite while maintaining self-healing capability. Both cement and polymer-cement composite samples were then cured in a 2 L autoclave with 30 mL of water at 200 °C for 5 days. In the sample preparation, we used Class H cement, supplied by LaFarge from the Joppa Plant, and Silica flour (200 mesh) from U.S. Silica. Sigma Aldrich supplied poly(ethylene glycol) diglycidyl ether (PEO) (250 g/1 equivalent epoxide) and pentaerythritol tetrakis (3-mercaptopropionate) (4SH), while Thioplast EPS 25 (EPS 25) (640 g/1 equivalent epoxide) was supplied by Akzo Nobel.

2.2. Exposure to CO_2 environment and post-exposure sample preparation

The cured cement and polymer-cement samples were immersed in 1 wt.% NaCl brine and pressurized with 3000 psi of supercritical CO_2 at 250 °C for one month in triplicate. After the exposure, two polymer-cement composite samples were cut transversally into "hockey puck" shaped cylinders 0.5 cm thick using a diamond blade in a low-speed saw (Fig. 1 (E) and (F)). Then, these samples were further cut into $2 \times 2 \times 20$ mm parallelepiped samples for synchrotron based XRF measurements, using the same blade and saw speed. One side of the parallelepiped sample correspond to the external perimeter (exposed to CO_2/brine solutions) of the "hockey puck" sample which includes the reaction front. Water was used as the cooling fluid in both cutting and grinding/polishing the surfaces. The flat area of the samples was ground with 600 and 1200 grit silicon carbide papers. After grinding, a 1-micron lapping film was used to polish the flat cross-section surface, again using water as cooling fluid. No oils or solvents were used to avoid interactions with the polymer. Both the reacted samples, as well as an unreacted (control) sample, were prepared for analysis.

2.3. Material characterizations

2.3.1. SEM and EDX

The surface morphology and chemical composition of the samples were investigated using a FEI Quanta 600 FEG environmental scanning electron microscope (FE-SEM) equipped with energy dispersive x-ray spectroscopy (EDS). The backscatter electron (BSE) detector was placed at a working distance of 10 mm with voltages of 10 kV and 20 kV to accommodate sample charging. Samples were sectioned and polished beforehand to get the optimum surface imaging before and after exposure.

2.3.2. XRF and XANES

The XANES spectrums at the Fe edge and associated X-ray fluorescence (XRF) mapping were collected at the SRX beamline (5-ID) in the National Synchrotron Light Source II (NSLS-II) at Brookhaven National Laboratory. The energy of the incident beam was 9.6 keV, with the beam size of 1×1 μm². Both Ca and S XANES spectrum was collected at the 13-ID-E beamline in the Advanced Photon Source (APS) at Argonne National Laboratory. The Ca maps were collected at energy of

4.5 KeV while S maps were collected at energy of 2.58 KeV. The data was reduced and analyzed using Athena software package, and the chemical compositions were calculated using the linear combination fitting.

2.3.3. X-ray microtomography

To obtain 3D volume data at up to $20 - 50$ μm resolution on sections of cement cores, an X-ray CT instrument, Nikon XTH 320/225 was used. The 3D data was then viewed as sliceable images and analyzed for structural and density changes on the computer. To this end, high-resolution microtomography images were collected on cement samples before and after CO_2 exposure. The X-ray Computed Tomography (XCT) scans were performed at 90 kV and 350 μA x-ray power. During the scans, samples were rotated with momentary stops between each angular step to collect each projection without ring artifacts. A total of 3200 projections were collected over 360 degrees with an exposure time of 500 ms per projection. The images were collected at an isotropic voxel resolution of 12.9 μm, resulting in 32-bit grey-scale images. Reconstruction of the volume data was carried out using CT Pro 3D (Metris XT v2.2, Nikon Metrology). The reconstructed 32-bit images were further processed in Fiji/ImageJ (Image Processing and Analysis in Java; http://imagej.nih.gov/ij/ (2017)) as image stacks. After converting the data to 8-bit to reduce computation time, the image brightness and contrast were adjusted to maximize contrast between cement, polymer, and air components. It was found that the "Auto" setting adjustment in ImageJ's Brightness/Contrast option worked well to enhance phase contrast. The volume of interest was reduced by cropping the stacks to either $500 \times 500 \times 500$ or $750 \times 750 \times 500$ pixels to exclude outside air from the segmentation while keeping the useful data volume maximum. The image stacks were filtered using the Median 3D filter option with kernel size 2.0 to make the components more homogeneous in grey-scale intensity, thereby improving phase boundaries for the segmentation step. The three components of interest (cement, polymer, and air) were segmented using the machine learning-based Trainable Weka Segmentation 3D plugin in Fiji (part of ImageJ). This segmentation showed that the phase contrast (grey-scale intensity difference) between the three components was sufficient to segment each component successfully at a resolution similar to the voxel size. Finally, the segmented volume false-colored according to the three components was exported as a new volume/image stack in 24-bit RGB format and volumetrically analyzed for the volume fraction of each component using VG Studio Max 2.1 (Volume Graphics GmbH, Heidelberg Germany). This software was also used to create the visualizations from the CT data shown later. The different colors of the segmentation classes show where the treatment affects the samples.

2.3.4. Specific surface area analysis

Surface area was determined using the Micrometrics Surface Area Analyzer (Model 2020 Micrometrics Instrument Corp., Norcross, Ga). A detailed description of the procedure to determine surface area is presented in the operating manual (Micromeritics, 2006). Cement samples were broken at the edge and sieved to $0.5 - 1$ mm size before analysis for specific surface area. To perform the analysis, cement samples were first air dried followed by placing them in a glass tube and connecting it to the evacuation port. The samples were out gassed for three hours at 150 °C and at a pressure of 3 μm Hg to remove physisorbed water. The instrument isolates the vacuum pump from the sample every five minutes to determine pressure levels. If the pressure change is below 2 μm Hg, the sample is considered clean and dry. The next step consisted of carrying out adsorption isotherm of nitrogen at -196 °C to determine the surface area of the sample. The approach is based on the multi-point Brunauer–Emmett–Teller (BET) adsorption equation using nitrogen. The equipment uses an imbalance of atomic forces on the surface of a clean evacuated solid sample to attract gas molecules. The gas molecules collide with the surface of the analyte and either are adsorbed onto the surface or bounced off. The molecules that adsorb

onto the material's surface no longer are present in the gas phase, reducing the gas pressure. The number of molecules adsorbed can then be determined by the volume of the sample container, temperature, and the change in pressure. From the number of adsorbed molecules, the surface area is calculated.

2.3.5. Mechanical properties

The compressive strength tests were performed on cement monoliths with an average length of 8.2 ± 0.5 cm and diameter of 2.5 ± 0.03 cm, where triplicate measurements were done for every sample. Samples were cured for at least 5 days using ASTM C39/C39M-15a standard methods and then the monolith ends were cut perpendicular to the length to provide a flat surface and minimize the point loading during testing. The MTS instrument, Model 312.31 servohydraulic frame with a 55-kip actuator and load cell, was used to test the samples at loading rate of 0.24 MPa/s. Cardboard shims were placed between the plate and sample to adsorb potential point loading from sample defects.

3. Results

3.1. Visual evidence of cement alteration after exposure to CO_2

After scCO$_2$ exposure, a white precipitate (CaCO$_3$) was observed on both the control (Class H) and the polymer-cement composite samples. The precipitate was significantly more dominant on the control cement samples (Fig. 1, bottom). As shown in previous studies, all cements showed a change from original grey cement color to a brown-orange color on the outer surface (Fig. 1(C) and 1(D)) (Kutchko et al., 2007; Kutchko et al., 2008; Kutchko et al., 2009b). Also, a clear reaction front, similar in width for both control and composite cements on the cross-sectional samples, was observed though the reaction front colors were different (Fig. 1(E) and (F)).

3.2. Cement surface morphology

To evaluate the changes in the surface structure of the control and polymer-composite cements, the altered materials after CO$_2$ exposure were studied using SEM and EDS (Figure S1 and S2 in Supplementary Information). When the control sample (no polymer) was exposed to CO$_2$, a reaction rim formed at the edge of the sample, which is heavily pitted as it appears to have undergone significant carbonation related dissolution, as shown in Fig. 2(A). The reaction rim is approximated by the dashed line in the figure. The breakdown of the microstructure in the rim indicates a potential loss of structural integrity. Further EDS measurements were done to study chemical changes after CO$_2$ exposure (see elemental spectra in Figures S1 and S2 in Supplementary Information). Fig. 2(B) shows that the pores along the rim are filled with calcium carbonate precipitates. As you move further into the sample, "popcorn carbonation" appears as a patchwork of carbonated cement and decalcified cement throughout the interior of the cement matrix. This phenomenon, which is known as a bicarbonation, is shown in Fig. 2(C). Gypsum was found throughout the sample and precipitated in the pores as shown in Fig. 2(D).

In the polymer-cement composite samples, the porosity appeared to increase adjacent to the reaction rim as shown in Fig. 3(A) though not as pronounced as in the control cement (Fig. 2(A)). The origin of the larger number of pores in polymer-cement composites could be due to the higher water content in polymer-cement slurries required to maintain the desired slurry flowability. This excess water may then be released during the curing process at high temperature and the pores formed filled with polymer (Ian Childers et al., 2017). The cement matrix showed calcium carbonate precipitation throughout the sample and in the pores as shown in Fig. 3(B), spots i and ii. Fig. 3(C) shows the calcium carbonate precipitate filling a pore in the cement matrix, which was further confirmed with the high Ca concentration in the EDS

measurements of spot ii and shown in Figure S2(B). Silica was also observed in the cement matrix as shown in Figs. 3(B) and Figure S2, spot iii. Secondary regions of calcium-rich and decalcified paste are present throughout the interior in a way reminiscent of popcorn carbonation as shown in Fig. 3(D). EDS measurements showed that the region contains calcium-rich patches with small flecks of sulfur-rich and iron-rich particles as shown in Fig. 3(D) and Figure S2, spots iv and v. These particles are too small to confirm by morphology but are consistent with formation of gypsum and pyrite based on XANES analysis, as discussed Section 3.3.

3.3. Elemental distribution and chemical states

XRF mapping was conducted on both the control and polymer-cement composite samples to elucidate the changes in elemental distribution as a result of carbonation. Fig. 4 shows the Ca XRF mapping for cement before (Fig. 4(A)) and after polymer addition (Fig. 4(B)) and CO$_2$ exposure (Fig. 4(C) and (D)). The control cement shows a uniform distribution of Ca on the surface with several scattered high concentration spots (Fig. 4(A)). In addition, void space observed is very limited, indicating a dense microstructure. On the other hand, the polymer cement (Fig. 4(B)) showed a higher void space as compared to control cement with much more localized Ca concentration especially around the pore structures as shown in Fig. 4(B).

The exposure to CO$_2$ was found to alter the elemental distribution of both control and polymer-cement composites, leading to the formation of three distinct zones in both cement samples. Starting from the rim is Zone 1 with a porous rim where calcium is leached out of the cement along with silica. Zone 1 is followed by Ca carbonate precipitate ion (Zone 2), where precipitation of CaCO$_3$ is evident from the high Ca concentration in the XRF maps. Neighboring Zone 2 is Ca depleted Zone 3, indicating that calcium hydroxide starts to break down and leads to migration and precipitation of Ca to Zone 2. Zone 3 is followed by unaltered cement where no precipitation and dissolution are observed. This is illustrated in Fig. 5 and will be described in detail in the Section 4, Discussion.

From the XRF observations, the carbonation front on the control (Fig. 4(C)) and polymer-cement composites (Fig. 4(D)) seem comparable, and there was no additional impact noted due to the presence of polymer, indicating that polymer-based cement retains similar chemical reactivity as control cement and should be comparably resistant to CO$_2$-rich environments.

Micro-XANES was used to study the qualitative changes in the chemical compositions and oxidation states adopted by S and Fe in control and polymer-cements after carbonation at a few sites on every sample. The sites selected for measurements were hotspots and spots with minimum concentration of S and Fe. The XANES analysis of the S edge was found to differ dramatically with exposure as well as position as shown in Fig. 6(B). CaSO$_4$ was found on the surface of the cement after exposure to CO$_2$. This is consistent with the SEM/EDS observation and indicates the presence of gypsum in the as-made cement (Thaulow and Jakobsen, 1997). When the polymer was added, CaSO$_4$ was found in higher percentages in the pores in the cement matrix, along with pyrite as seen in Fig. 6 (position *ii*) and summarized in Table S1. On the other hand, the CaSO$_4$ was found in minute amounts (≤ 5%) on the surface mixed with dominant chemical structure of pyrite as seen in Fig. 6 (position *i and iii*) and as summarized in Table S1. This is consistent with the small amount of gypsum (3–5%) added to the unhydrated cement powder to prevent flash setting. Any additional gypsum precipitation may likely be attributed to the excess sulfur available in the unreacted cement and in the polymer-cement composites, which reacts with both Ca and Fe (Ian Childers et al., 2017; Jupe et al., 2008; Liu et al., 2015).

In the Fe-edge micro-XANES analysis, measurements showed that the control cement contains ferrihydrite, while a mixture of ferrihydrite and goethite was observed after exposure to CO$_2$. However, in the case
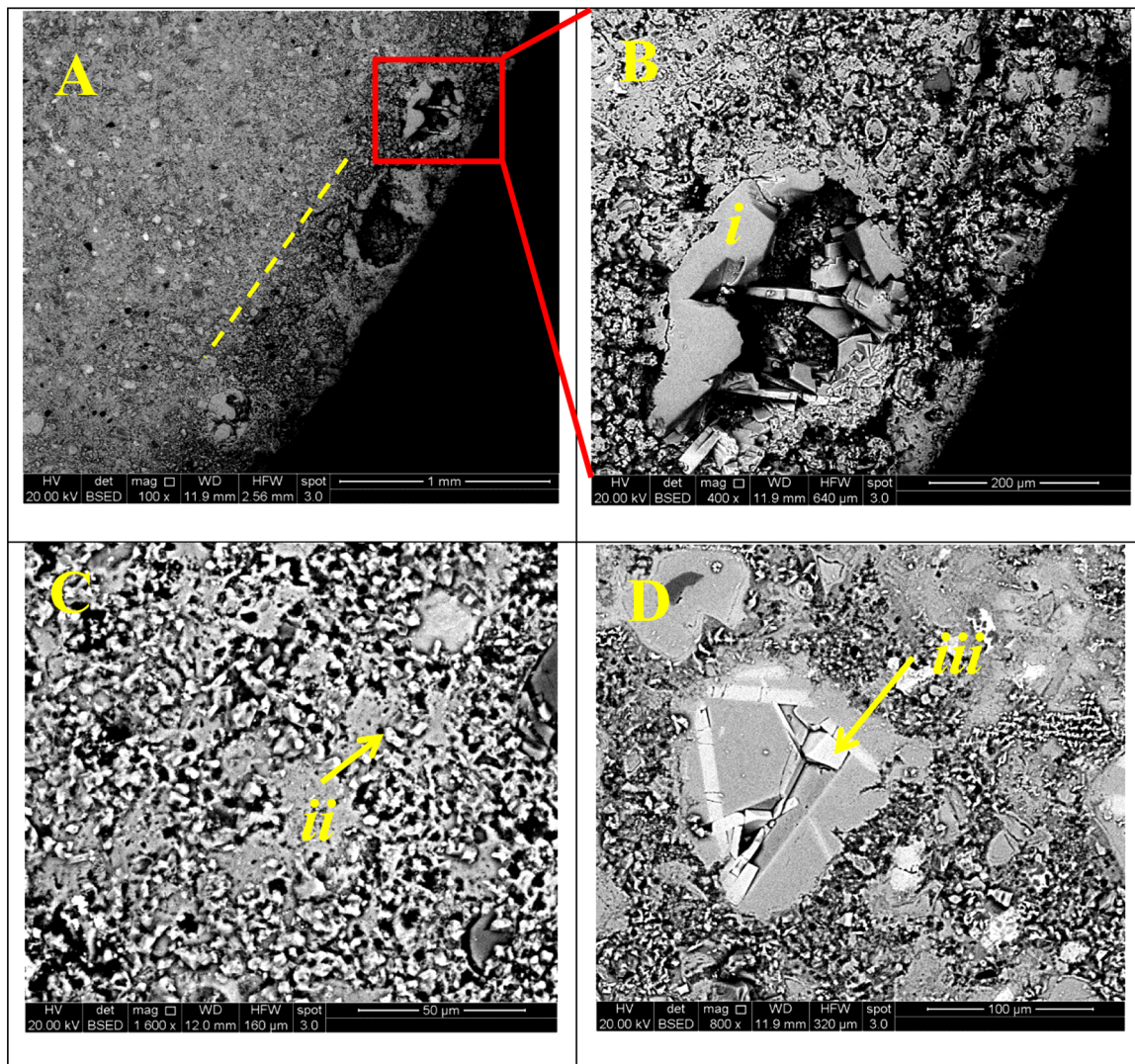
Fig. 2. SEM backscattered image of control cement exposed to CO_2: (A) the reaction rim showing high porosity and alteration throughout the entire sample, (B) the reaction rim showing high porosity and calcium carbonate precipitation and dissolution, (C) popcorn carbonation *(ii)*, and (D) gypsum and calcium carbonate. For EDS analysis, please refer to Figure S1.

of polymer-cement exposed to CO_2, siderite was observed along with ferrihydrite and goethite, which supports the carbonation of the cement as shown in Fig. 7. The spatial variations observed and the concentrations of ferrihydrite, goethite, and siderite varied from one point to another as summarized in Table S2.

3.4. X-ray microtomography studies

To evaluate the changes in microstructure and porosity, control and polymer-cement composites were studied using X-ray microtomography both before and after CO_2 exposure (Figs. 8–10). It was observed that polymer-cement composites had higher open porosity (Fig. 8 (A) and (B)) with 9.6 $\pm$ 0.9 % of void space (Fig. 9 (C) and (D)) as compared to control cement with 6 $\pm$ 1% porosity (Fig. 9 (A) and (B)). It is important to note that the resolution of our XCT data was limited by the 12.9 μm voxel size. Therefore, pore sizes smaller than the resolution limit may also be present. It is also expected that further micro-porosity may have been lost due to noise and phase contrast limitations. However, the total volume fraction of the polymer that resulted from the segmented data is in agreement with that was expected based on the sample preparation recipe. As described earlier, the greater open porosity in the polymer-cement composites can be

attributed to the additional (unreacted) water to maintain the desired slurry flowability and it is in agreement with SEM observations regarding the microstructure. It has been previously reported that the polymer is hosted on these homogeneously distributed pores.

Control cement samples (no polymer) upon exposure to CO_2 show a significant decrease in void volume (~ 70 % reduction) (Fig. 10 (B)) potentially due to the reaction of CO_2 with $Ca(OH)_2$ around the voids with a simultaneous increase in the material's volume in the air pockets due to the formation of $CaCO_3$. Polymer-cement materials also undergo a decrease in void volume fraction (~ 50 %) with a simultaneous decrease in polymer volume fraction (Fig. 10 (D)). It is observed that overall the polymer-cement composite maintains a higher and relatively homogeneous porosity after CO_2 exposure compared to control cement. The control cement exhibits very heterogeneous void distribution consisting of large voids throughout the cement matrix (Fig. 10 (A) and (B)).

3.5. Specific surface area analysis

Cement samples were broken at the edge and sieved to $0.5 - 1$ mm size to (1) minimize the contribution of higher surface area powder and (2) warrant contribution to surface area by the pores (significantly
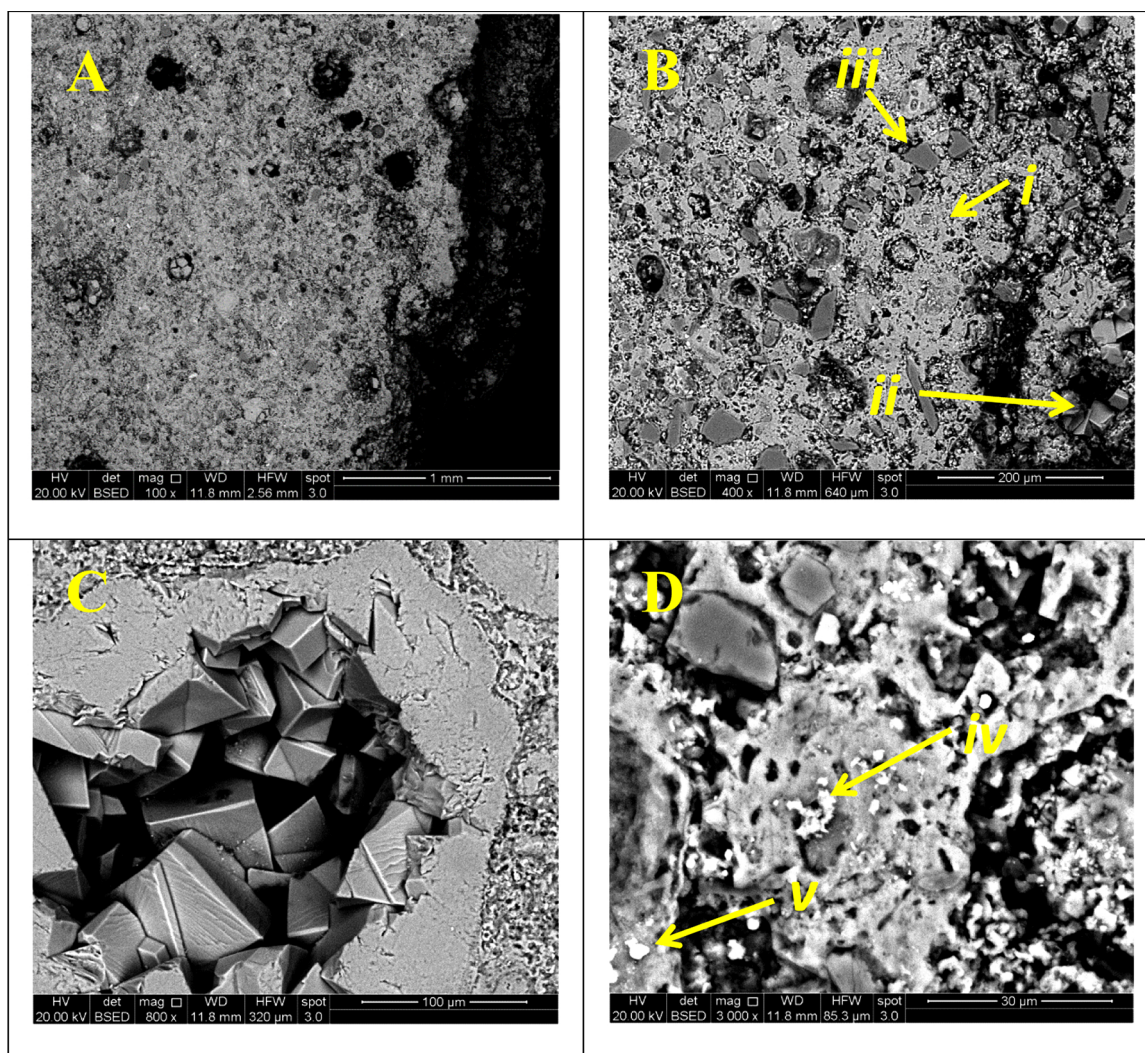
Fig. 3. SEM backscattered image of polymer cement exposed to CO_2: (A) the reaction rim showing pores and alteration throughout the entire sample, (B) calcium carbonate precipitates (*i, ii*) and silica *(iii)* along the rim of the cement sample, (C) calcium carbonate precipitates in a pore, and (D) popcorn carbonation and iron-rich particulates (possibly pyrite) *(iv, v)*. For EDS analysis, please refer to Figure S2.

smaller than grain sizes). The surface area values were obtained with an uncertainty of 6% (one standard deviation) and resulted in values of 15.9 m^2/g and 16.1 m^2/g for unexposed base cement and unexposed polymer-cement composites, respectively. After exposure to CO_2, the surface area decreased for both cement materials showing 12.0 m^2/g for base cement and 11.1 m^2/g for polymer-cement composites.

3.6. Mechanical properties

When the control cement sample was exposed to CO_2, its compressive strength doubled, as shown in Fig. 11, potentially associated to conversion of $Ca(OH)_2$ to Ca and Ca-Si carbonates. In addition, the base cement samples become very brittle and difficult to manipulate (Fig. 12). On the other hand, exposure of polymer-cement composites seems to reduce the compressive strength values by approximately 30 % though this difference could be simply due to sample variability.

4. Discussion

CO_2 is known to affect the integrity of conventional wellbore cement due to the formation of carbonates, which render the cement material brittle (Kutchko et al., 2007; Kutchko et al., 2008; Kutchko et al., 2009b). This conclusion was no different in the present work

although polymer-modified cements seem to offer a key advantage as will be described later.

Both SEM and EDS results of the control cement samples after exposure to CO_2 are consistent with the formation of calcium carbonates (Kutchko et al., 2007; Kutchko et al., 2008; Kutchko et al., 2009b; Busch et al., 2008; Zhanga et al., 2014). A porous structure was observed and is associated with the reaction front, which can be explained by the degradation mechanism proposed by (Kutchko et al. (2008)). In brief, high pressure CO_2 forms carbonic acid (Eq 1) in aqueous solution leading to acidic pH values (pH = 3-5) that vary in range depending on CO_2 concentration (pressure) and temperature. At the cement surface, the presence of carbonic acid begins to lower the pH, which initially has an approximate value of 12 due to the presence of $Ca(OH)_2$ in the cement matrix. After diffusion of acidic carbonated fluid through the cement matrix, the $Ca(OH)_2$ dissolves (Eq 2) leading to an increase in porosity in Zone 1 and to the enhanced leaching of Ca out of the cement matrix (see Figs. 4 and 5). In Zone 2, the precipitation of Ca^{2+} as calcite takes place along with diffusion of carbonated fluid towards the cement matrix (Eq 3). This can be clearly observed in both XRF (Fig. 4 (C) and (D)) and SEM data (Figs. 2 and 3). Such calcite formation occurs inside the pores with the associated reduction in porosity as well as an increase in compressive strength (Kutchko et al., 2008).
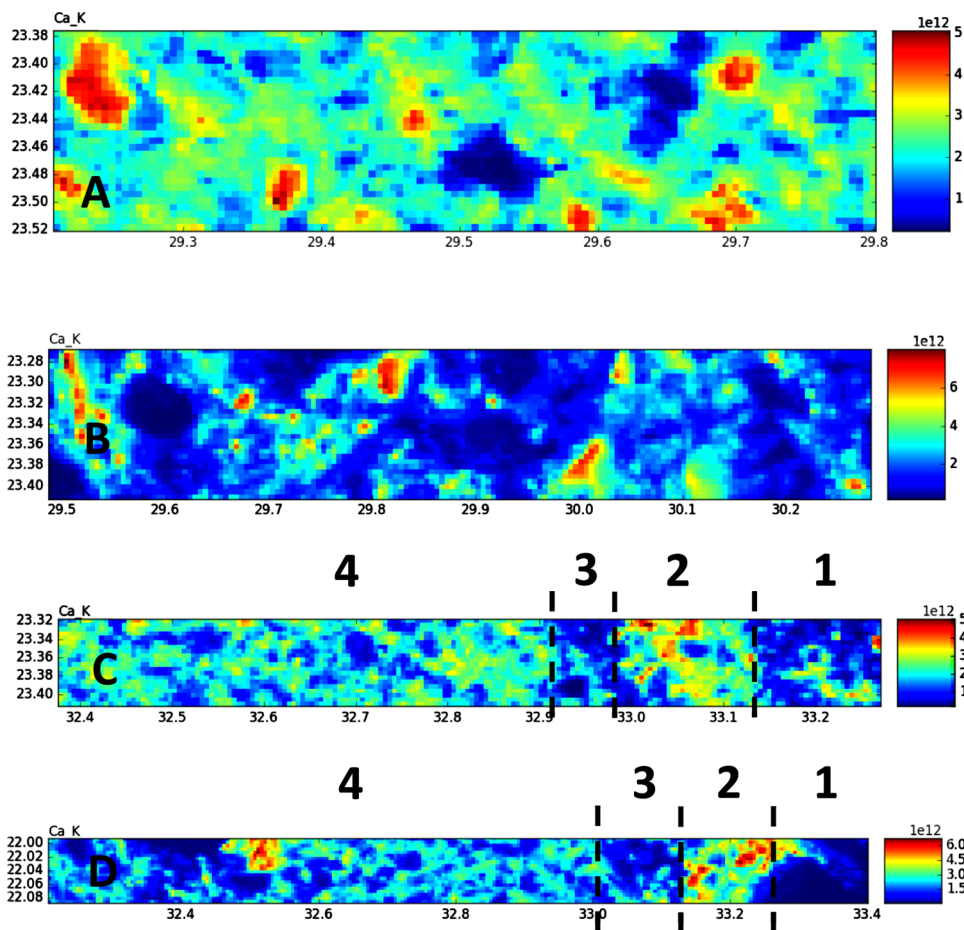
$$CO_2(aq) \ + \ H_2O \rightarrow H_2CO_3 \ (aq) \qquad (1)$$

Fig. 4. XRF Ca map for (A) unexposed control cement sample (no polymer), (B) unexposed polymer-cement composite (10 wt% polymer), (C) control cement (no polymer) exposed to CO_2, and (D) polymer-cement composite (10 wt% polymer) and CO_2 exposure. Both x and y axis are in mm.

The regions can be described as follow: (1) reaction front, (2) high carbonation zone, (3) Ca depletion zone, and (4) unaltered cement. The map was collected at energy of 9.6 KeV.
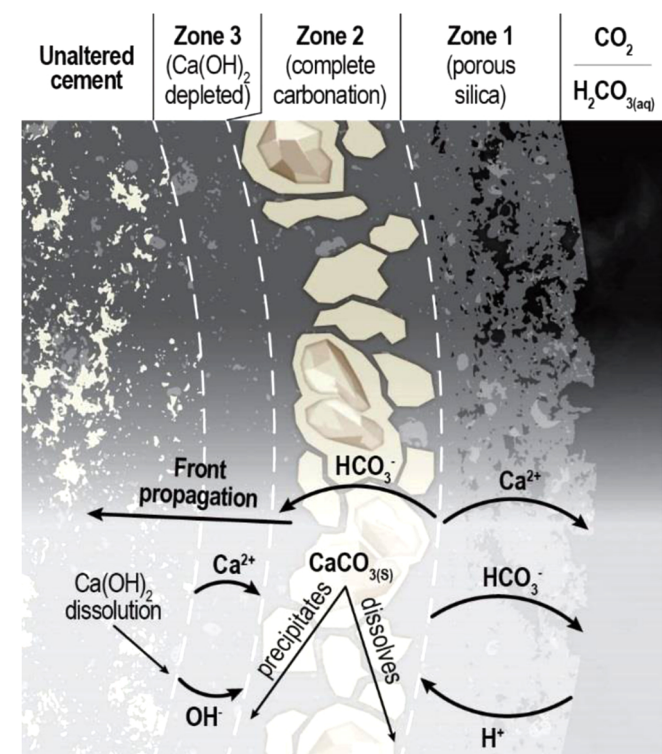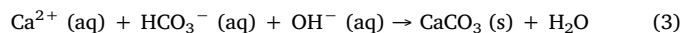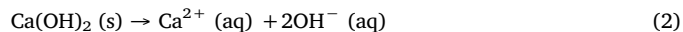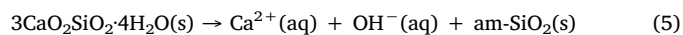

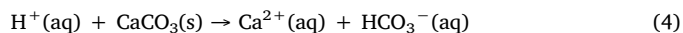**Fig. 5.** Schematic showing the dissolution and calcium migration and formation of distinct zones in the cement after exposure to CO_2.

$$Ca(OH)_2 \text{ (s)} \rightarrow Ca^{2+} \text{ (aq)} + 2OH^- \text{ (aq)} \qquad (2)$$

$$Ca^{2+} \text{ (aq)} + HCO_3^- \text{ (aq)} + OH^- \text{ (aq)} \rightarrow CaCO_3 \text{ (s)} + H_2O \qquad (3)$$

This dense calcite-filled microstructure in Zone 2 could, in principle, provide a temporary barrier to the acid attack due to its lower permeability, if the reaction front stopped at Zone 2 (Fig. 5). However, once the $Ca(OH)_2$ depletes, $CaCO_3$ begins to dissolve and forms carbonate ions. As $Ca(OH)_2$ depletes, the pH drops below 11 and the carbonate ion concentration decreases with bicarbonate ions becoming the dominant species. Water soluble calcium bicarbonate (Eq 4) readily diffuses into the cement matrix and results in a formation of large, non-interlocking calcium carbonate crystals. These calcium carbonate crystals can be identified by their distinct "popcorn" shape. Popcorn carbonation, which is determined by the concentration balance between calcium hydroxide and CO_2, has a negative effect to cement since these crystals act as sand grains rather than as a binding agent. Furthermore, after dissolution of $CaCO_3$, the cement loses its ability to buffer the pH and $3CaO_2SiO_2 \cdot 4H_2O$ (C-S-H) paste is converted to highly porous amorphous silica (Eq 5) (as observed by SEM), leading to the formation of a second calcium-depleted Zone 3 (Fig. 5). This highly porous amorphous silica layer is very weak in strength and lacks structure. It is the cause of cement weakening after very long CO_2 exposure times (years).

$$H^+ \text{(aq)} + CaCO_3(s) \rightarrow Ca^{2+} \text{(aq)} + HCO_3^- \text{(aq)} \qquad (4)$$

$$3CaO_2SiO_2 \cdot 4H_2O(s) \rightarrow Ca^{2+} \text{(aq)} + OH^- \text{(aq)} + am\text{-}SiO_2(s) \qquad (5)$$

Although the above-described reactions were observed in both base cement and polymer-modified-cement, the concentration of popcorn carbonation seems lower in the polymer-modified cement (Fig. 3(D)) as
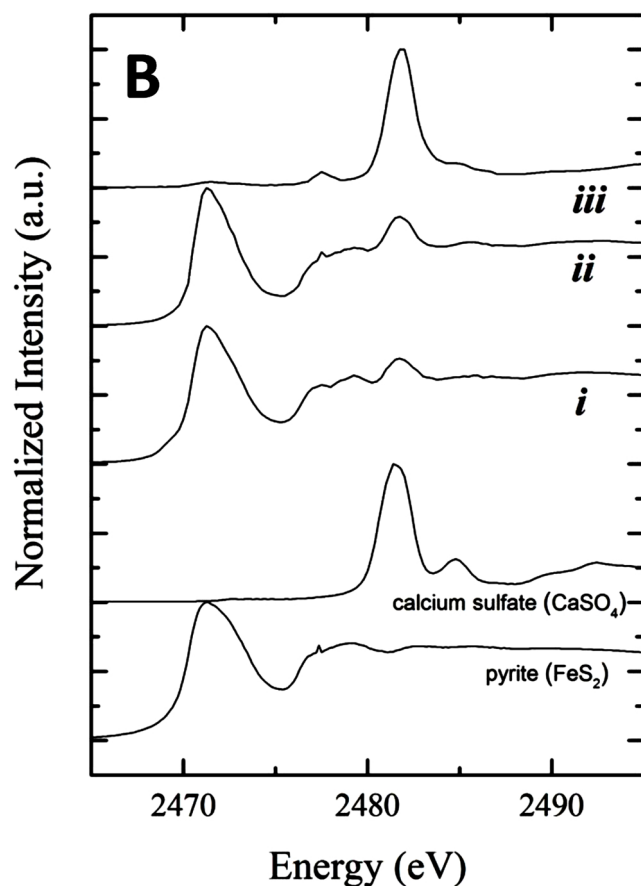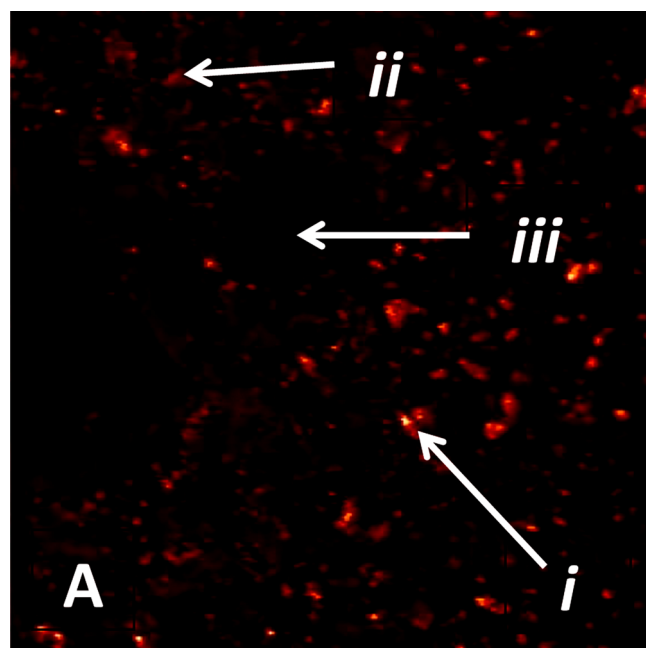
Fig. 6. (A) XRF S map for polymer-cement composites with 10 wt% polymer after CO_2 exposure. The map was collected at energy of 2.58 KeV. (B) XANES spectra at the positions shown in (A).

compared to the base cement (Fig. 2 (C)).

Besides the product of carbonation reactions described above, minor amounts of other compounds were found to be present in the reaction front as compared to the unreacted (bulk) cement for both base and polymer-modified cements. For example, although gypsum is present in $5-8$ wt% in wellbore cement powder, secondary gypsum formation was observed in the reaction front for both base cement and polymer-modified cement and could be due to the oxidation of pyrite, which was also present in both cements. Oxidation of pyrite in cement in a high-temperature carbonated brine is expected and has been shown to lead to the formation of sulfuric acid and cement deterioration. In the presence of oxygen and moisture, pyrite will oxidize to ferrous sulfate and sulfuric acid. The free sulfuric acid will typically react with calcite present to produce secondary gypsum (Hewlett, 1998). However, further studies are needed to determine if oxidation will occur downhole in the wellbore environment. Therefore, although oxidation of pyrite is a serious problem on the surface (for example, acid mine drainage), it is unknown if it will be a problem downhole.

The presence of pyrite in both base cement and polymer-modified cement was observed in the XANES analysis. The presence of pyrite in cement observed here has been shown to be due to the interaction between the iron-rich compound ferrihydrite (C_4AF in cement notation) and sulfur present in the polymer. Previous *in situ* studies on cement and CO_2/H_2S interactions show the importance of pH to the redox reactions and subsequent mineral precipitation and dissolution that occur within the cement matrix (Kutchko et al., 2011). This is especially true due to the strong pH gradient from the interior to the exterior (rims) of the cement that occurs upon exposure to acidic environments, such as a CO_2-rich fluids under simulated storage conditions. Mineralogical changes, such as the conversion of ferrihydrite to pyrite, have been seen in other CO_2 exposure experiments with the addition of sulfur to the system (Kutchko et al., 2011; Jacquemet et al., 2008). The carbonation process brought about by the ingress of CO_2 rich fluid provides the right localized pH range in the cement matrix for the redox reaction to occur. Kutchko et al. speculated that the formation of pyrite can occur through multiple pathways, such as a "meta-stable intermediate" (Rickard and Luther, 1997) or the "polysulfide pathway" (Rickard and Luther, 1997; Schoonen and Barnes, 1991). Secondary gypsum formation in set cement is known to be highly deleterious in surface applications of cement due to the fact it is an expansive mineral (Kutchko et al., 2015). However, it appears that the gypsum content is related to the amount of gypsum added to the unhyrdated cement powder and is likely formed during the hydration process. Secondary gypsum formation is dependent on pH as well as temperature and amount of sulfur (Kutchko et al., 2015).

After CO_2 exposure, an orange-brown coloration was observed due to the dissolution of $Ca(OH)_2$ and silica, leaving behind more concentrated ferrite phase at the surface. Qualitative XANES analysis shows that the Fe speciation changes upon exposure to CO_2. In the case of the base cement, ferrihydrite is still present but goethite is also observed. On the other hand, goethite and siderite were observed in the polymer-cement samples post$-CO_2$ exposure while no ferrihydrite was found in the sample areas analyzed. The conversion of ferrihydrite to goethite involves complete rearrangement of the crystal structure from poorly ordered $FeO_3(OH)_3$ octahedral units in the unstable ferrihydrite phase to highly ordered edge-sharing octahedral double chains in goethite. This conversion usually occurs via a dissolution and reprecipitation mechanism, where initially ferrihydrite dissolves (Das et al., 2011; Yee et al., 2006). Formation of siderite has been shown to occur as the result of reduction of Fe^{3+} to Fe^{2+} in hematite followed by reaction with CO_2 to form iron carbonate (Romanov et al., 2015). In our work, it seems like either (or both) ferrihydrite and goethite undergo a similar reaction path, though there is no precedent literature supporting this observation. The fact that siderite was only found in the polymer-cement samples post$-CO_2$ exposure and not in the base cement samples post exposure is not understood and requires more detailed studies. It is also important to mention that micro-XANES was performed where a few spots were measured to study the chemical structure of the reaction products qualitatively. Therefore, the XANES results may not be representative of the entire sample.
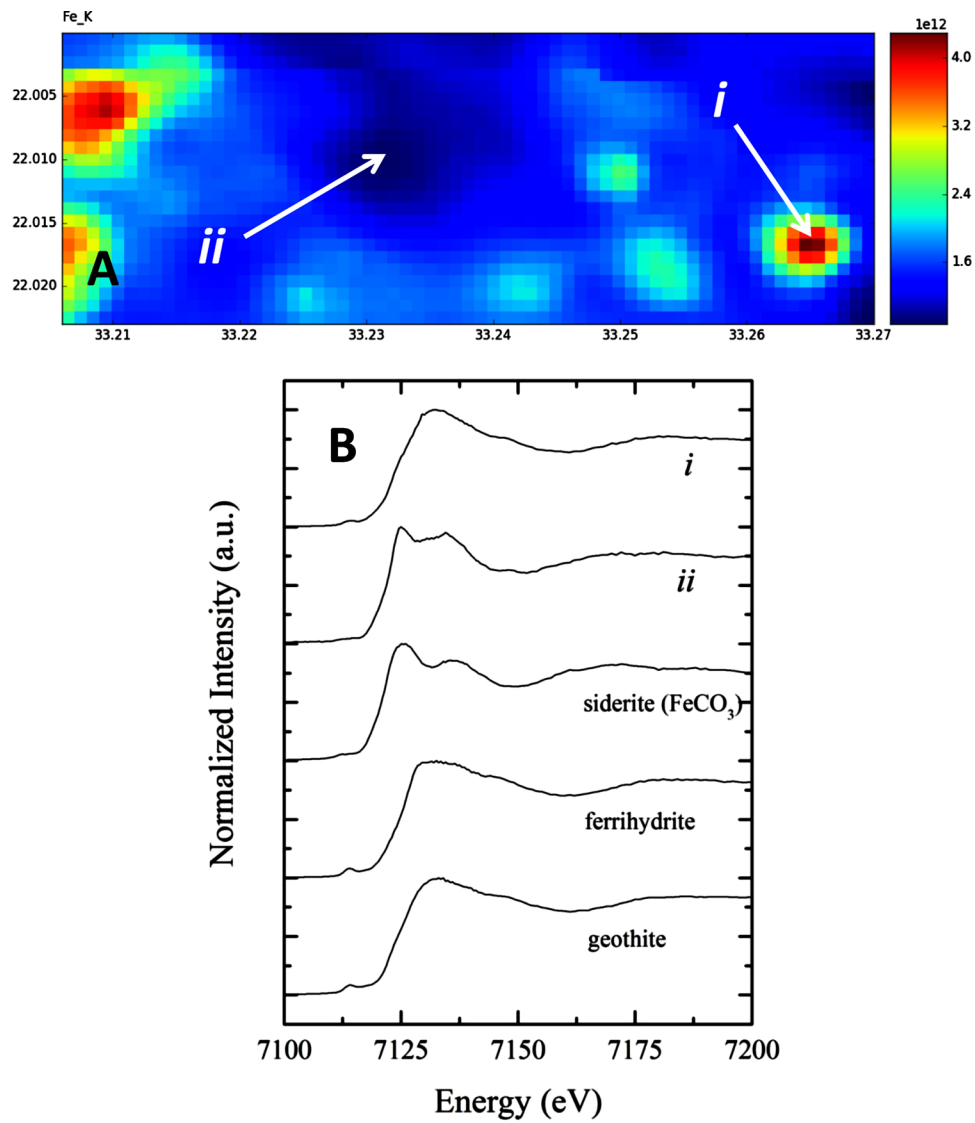
Fig. 7. (A) XRF Fe map for polymer-cement composites with 10 wt% polymer after CO_2 exposure. The map was collected at energy of 4.58 KeV. Both x and y axis are in mm. (B) XANES spectra at the positions shown in (A).
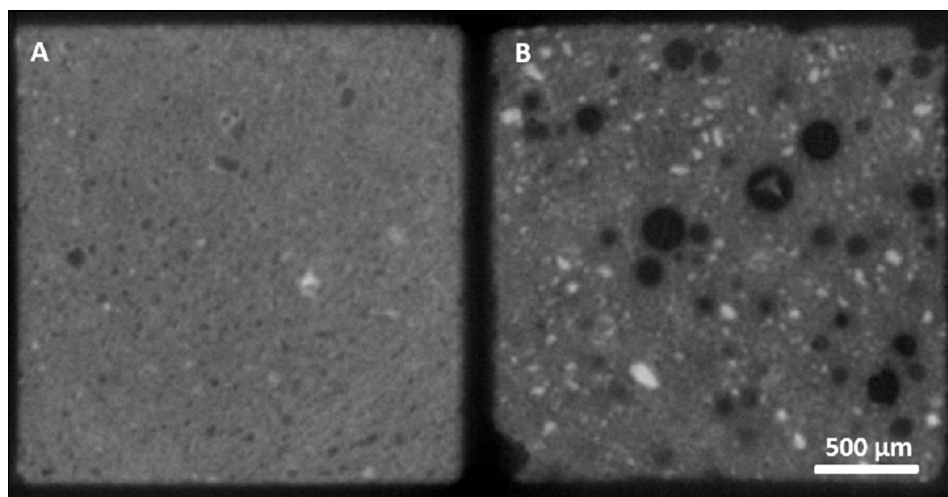

Fig. 8. X-ray micro-tomograms of (A) control cement and (B) composite cement (10 % polymer).
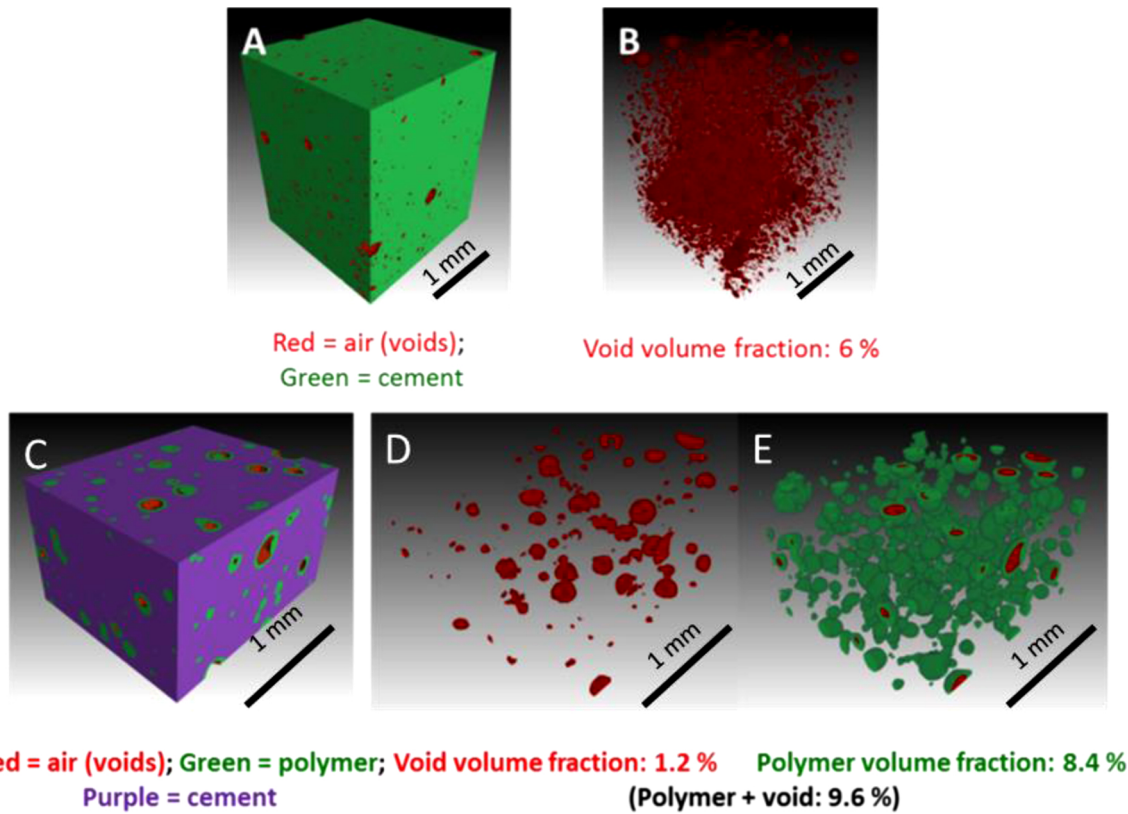
Fig. 9. X-ray computer tomography (XCT) with false color classification of (A) control cement, (B) control cement void volume fraction = 6 ± 1 %, (C) composite cement (10 % polymer), (D) composite cement void volume = 1.2 ± 0.2 %, and (E) void plus polymer volume fraction of composite cement = 9.6 ± 0.9 % (polymer only = 8.4 ± 0.8 %).
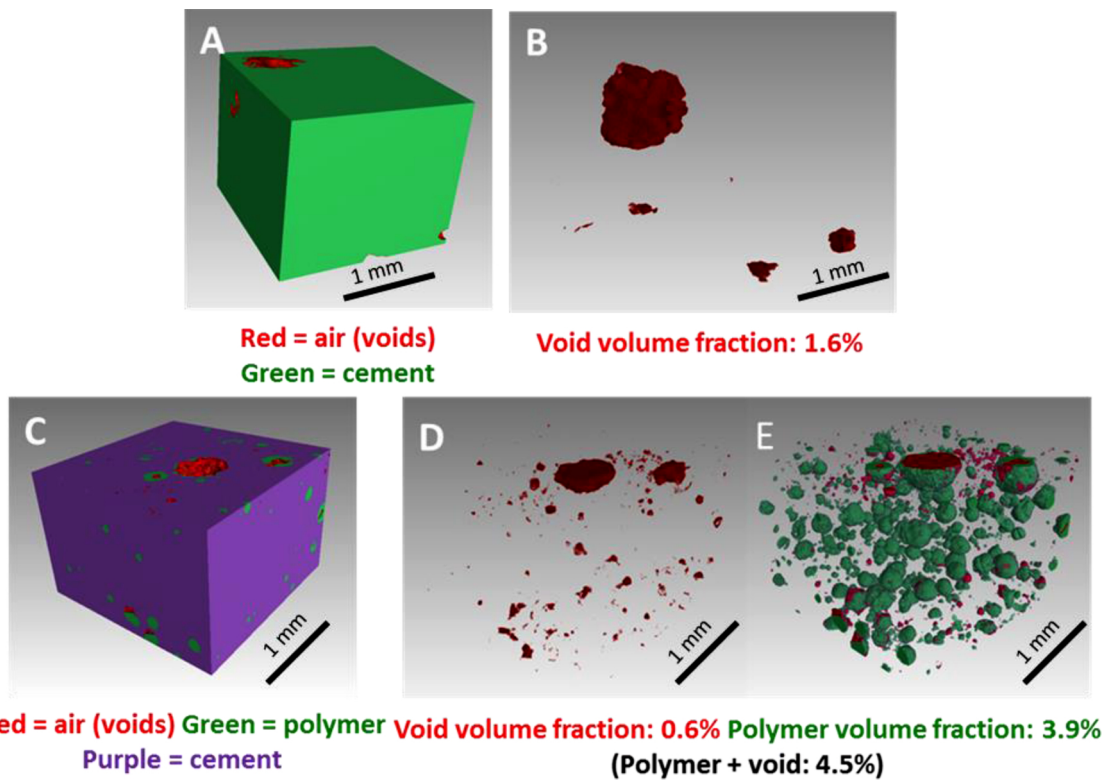

Fig. 10. X-ray computer tomography (XCT) with false color classification after samples has been subjected to high-pressure, high-temperature CO_2/brine exposure of (A) control cement, (B) control cement void volume fraction = 1.6 ± 0.2 %, (C) composite cement (10 % polymer), (D) composite cement void volume = 0.6 ± 0.1 %, and (E) void plus polymer volume fraction of composite cement after exposure to CO_2 = 4.5 ± 0.7 % (polymer only = 3.9 ± 0.6 %).
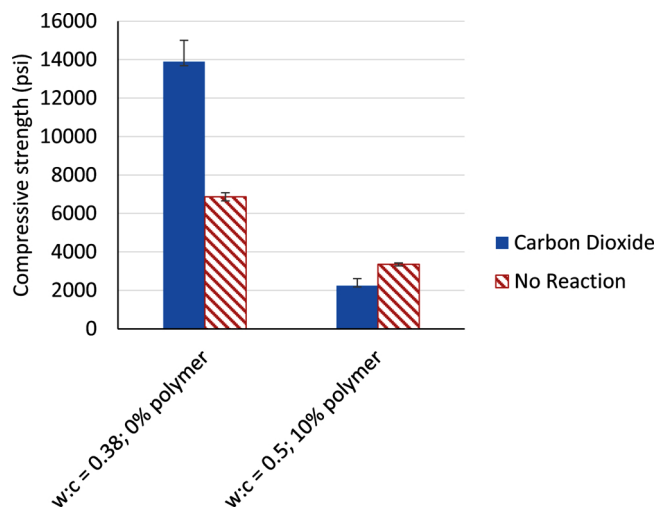
Fig. 11. The compressive strength of control and polymer-cement before and after CO_2 exposure.

In general, polymer-modified cements seem to react chemically similar to the control cement sample despite its higher porosity. Such similarity in reaction could be due to the presence of polymer in the pores that partially buffer the cement reaction with CO_2 (Figs. 9 and 10). In an attempt to understand the role that the polymer plays in the cement in the presence of CO_2, X-ray microtomography was carried out on conventional cement and polymer-modified cement samples before and after exposure to high-pressure aqueous solutions of CO_2 enriched in brine. Results show that unexposed polymer-cement samples have 50 % greater pores as compared to conventional (base) cement (Fig. 9), in agreement with SEM and XRF results. By using image segmentation of the XCT data for the classification of components of different densities, it was found that many of the void spaces in the polymer-cement samples had an apparent density between that of the cement and air, which we identified as polymer. This can be observed in Fig. 9, where most of the voids are partially or completely filled with polymer and that the remaining void (free) space accounts for 1.2 ± 0.2 %. We speculate that although the polymers are evenly distributed across the cement matrix, they tend to nucleate around or inside air voids. Upon exposure to CO_2, the base cement shows a significant decrease in void volume (~70 % reduction), which was confirmed to be due to the reaction of CO_2 with $Ca(OH)_2$ around the voids. The product of this reaction is $CaCO_3$ which fills the air pockets. Similarly, the polymer-cement samples undergo a decrease in void volume fraction (~50 %) with a simultaneous decrease in the polymer volume fraction (Fig. 10 (D)). The reduction in polymer volume fraction is potentially due to the polymer making room to the higher density $CaCO_3$ formed by the
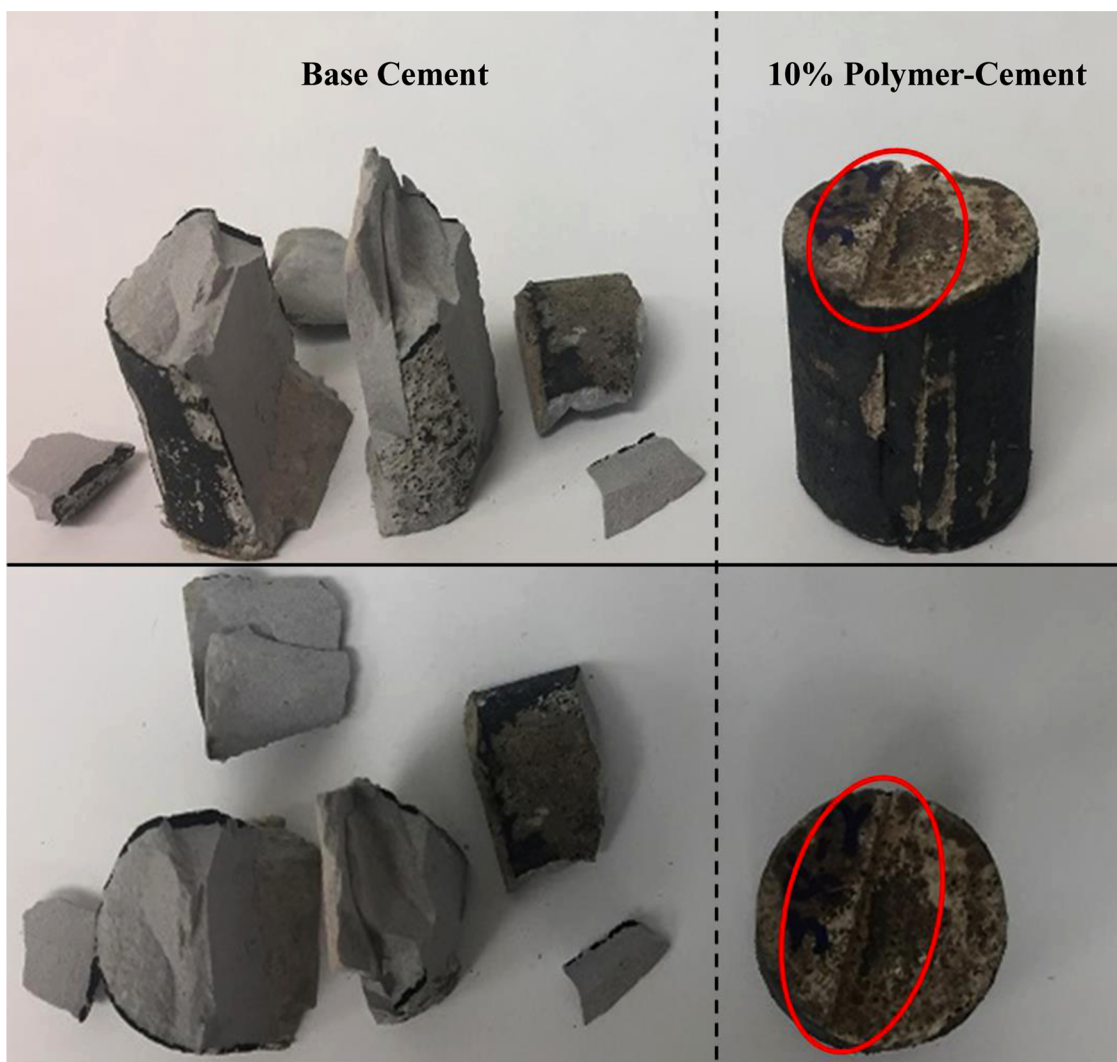

Fig. 12. Pictures of control (base cement) and composite cement taken after a healing event of a shear fracture. Note how more brittle base cement is irreversibly damaged in several pieces.

carbonation described above. As stated earlier, unlike base cement, the polymer-cement composite maintains a higher and relatively homogeneous porosity after CO_2 exposure with the majority of the pores filled with polymer (Fig. 10 (B) and (D)).

Surface area analysis results show similar surface area values for both base cement and polymer-cements, demonstrating that, although the cement composite has a larger concentration of pores, the pores are (1) not interconnected and (2) most of the pores are filled with polymer in the cement composite materials. The decrease in surface area from 15.9 and 16.1 m^2/g to 12.0 and 11.1 m^2/g in the base cement and polymer-cements, respectively, is a result of the reaction of CO_2 with Ca $(OH)_2$ precipitating $CaCO_3$ inside the pores as evidenced by SEM/EDS (Figs. 2 and 3 and Figures S1 and S2) and XRF analysis (Fig. 4).

The mechanical properties of the original (unexposed) samples were found to be significantly impacted by the addition of the polymer in their formulation. We found the base cement shows a comprehensive strength of 6500 psi versus a value of 3500 psi for polymer-cement composites (Fig. 11). Nevertheless, the compressive stress requirement is well above the required 1000 psi for wellbore applications, making polymer-cement composites suitable for their application in wellbore cement. After CO_2 exposure, polymer-cements maintained 70 % of the original compressive strength. The 30 % reduction in compressive strength is interpreted to be solely due to sample variability rather than a CO_2 exposure effect. On the other hand, the compressive strength of the control cement was found to increase to more than double its value with exposure to CO_2, making the material very brittle. This was observed when mechanically shocking the materials, the base cement $post-CO_2$ exposure completely crumbles while polymer-modified cements are ductile (Fig. 12). Such crumbling of base cement is likely due to the precipitation of mechanically stronger and brittle calcium carbonate as observed in SEM analyses, which also contributed to the reduction in porosity. In other words, CO_2 penetrates the porous cement matrix and reacts with $Ca(OH)_2$ forming $CaCO_3$, which contributes to the brittleness of the exposed cement.. Although it was observed in both the base cement and polymer-modified cement, CO_2 seems to have a much larger impact on the base cement mechanical properties. The two hypothesized reasons associated with the significant difference in compressive strength of $post-CO_2$ exposure between the base cement and polymer-modified cements are: (1) the presence of polymer evenly distributed in the cement matrix brings up flexibility to the material as previously reported, and (2) polymer may bring about a buffering effect reducing or retarding the reaction of cement components [in particular, $Ca(OH)_2$] with aqueous CO_2. The fact that compressive strength does not increase in polymer-cements could be due to the fact that the pores are mostly occupied by polymer decreasing the available volume for $CaCO_3$ precipitation upon reaction with $Ca(OH)_2$ during CO_2 exposure. This is clearly shown in Figs. 10 (D) as compared to Fig. 10 (B). It is worth mentioning that the fact that polymer-cement composites retains about 70 % of its mechanical strength make these materials suitable for structural support applications. Just recently, this team reported on the chemical and mechanical stability of this and other polymer-cement composites after exposure to high temperature (200 °C and 300 °C) for 10 and 30 days (Rod and Fernandez, 2020a, 2020b; Koech et al., 2020). The results of this work show that the polymer-cement materials were thermally stable and maintain their self-healing capabilities after 30 days exposure to elevated temperatures. These results were further confirmed by solid state ^{13}C Nuclear Magnetic Resonance spectroscopy (NMR) and X-Ray diffraction spectroscopy (XRD) as well as total organic carbon (TOC). TOC and ^{13}C NMR showed that the polymeric components were present in the polymer-cement composite indicating stability of the organic polymer at 200 °C after curing times of up to 30 days. Although this performance periods are insignificant compared to required wellbore lifetimes (average 30 years), they provide initial evidence that the self-healing cement materials are stable under harsh geothermal environments.

5. Conclusions

The application of synchrotron-based XRF and XANES methods complemented by microtomography and SEM analysis to investigate the performance of self-healing polymer-cement composite after exposure to a CO_2-rich environment is a powerful approach to gain mechanistic understanding of the carbonation process. Our study offers the fundamental knowledge needed to explain the performance of polymer-cement composites recently developed by Fernandez's group (Ian Childers et al., 2017; Nguyen et al., 2018) under CO_2-rich environments. In addition, mechanical strength studies are reported to validate the performance of polymer-cement composites under CO_2-rich environment.

In the presence of CO_2 in brine at subsurface conditions, both base cement and polymer-cement composites undergo the same interaction mechanisms with CO_2 but to different degrees. The exposure to CO_2 led to the formation of similar rim structures in the polymer-cement composites and the control cement. The observation of a brown-orange coloration in both base cements and polymer-cements is a result of the leaching of $Ca(OH)_2$ and SiO_2 in both materials, leaving behind a higher concentration of iron-based oxide in the surface of the samples. XRF studies showed a clear carbonation front in both base cements and polymer-cement composites with a Ca-rich carbonation zone and a neighboring Ca-depleted zone. Formation of secondary gypsum, goethite and siderite was observed after carbonation via qualitative micro-XANES analysis. The surface area decreased for both base cements and polymer-cements composites. However, the presence of the polymer in the pores seems to partially buffer the carbonation reaction despite the pore concentration abundance. The lower carbonation in polymer-modified cements was evidenced by (1) the lower concentration of popcorn carbonation observed in SEM micrographs as compared to base cement, (2) the significantly lower calcium carbonate precipitate mass surrounding the cement composite samples as compared to base cement, and (3) the fact that the polymer-cement composite samples maintain a higher and relatively homogeneous porosity after CO_2 exposure with the majority of the pores filled with polymer as compared to the nearly disappearance of empty voids in the control cement sample after CO_2 reaction represents a change for higher precipitations of Ca carbonates in the composites. Polymer-cement samples although show slight decrease in strength after exposure to CO_2 in brine, the strength of 3500 psi is well above the compressive strength requirement for wellbore cement (1000 psi), making polymer-cement composites suitable for their application in enhanced geothermal systems.

CRediT authorship contribution statement

Mohamed S. Elbakhshwan: Investigation, Methodology, Formal analysis, Data curation, Writing - original draft, Visualization. **Simerjeet K. Gill:** Conceptualization, Funding acquisition, Supervision, Writing - review & editing. **Kenton A. Rod:** Investigation, Formal analysis, Visualization, Writing - original draft, Writing - review & editing. **Emma B. Bingham:** Investigation, Formal analysis, Visualization. **Adriana L. McKinney:** . **Nicolas Huerta:** Investigation, Formal analysis, Visualization. **Christina L. Lopano:** Formal analysis, Writing - original draft, Visualization. **Barbara G. Kutchko:** Resources, Writing - original draft, Conceptualization. **Yu-chen Karen Chen-Wiegart:** Investigation, Data curation, Resources. **Chonghang Zhao:** Investigation. **Garth Williams:** Investigation, Resources. **Juergen Thieme:** Investigation, Resources. **Tamas Varga:** Investigation, Formal analysis, Visualization. **Lynne E. Ecker:** Project administration, Supervision. **Carlos A. Fernandez:** Conceptualization, Funding acquisition, Supervision, Writing - review & editing.

Declaration of Competing Interest

Acknowledgements

Appendix A. Supplementary data

Supplementary material related to this article can be found, in the online version, at doi:https://doi.org/10.1016/j.geothermics.2020.101932.

References

Bachu, S., 2000. Sequestration of CO_2 in geological media: criteria and approach for site selection in response to climate change. Energy Convers. Manage. 41, 953–970.

Barlet-Gouédard, V., Rimmele, G., Porcherie, O., Quisel, N., Desroches, J., 2009. A solution against well cement degradation under CO_2 geological storage environment. Int. J. Greenh. Gas Control. 3, 206–216.

Barlet-Gouédard, V., Rimmelé, G., Goffé, B., Porcherie, O., 2007. Well technologies for CO_2 geological storage: CO_2-Resistant cement. Oil Gas Sci. Technol. 62, 325–334.

Busch, A., Alles, S., Gensterblum, Y., Prinz, D., Dewhurst, D., Raven, M., Stanjek, H., Krooss, B., 2008. Carbon dioxide storage potential of shales. Int. J. Greenh. Gas Control. 2, 297–308.

Carey, W., 2013. Geochemistry of wellbore integrity in CO_2 sequestration: portland cement-steel-brine-CO_2 interactions. Rev. Mineral. Geochem. 77, 505–539.

Carroll, S., Iyer, J., Walsh, S., 2017. Influence of chemical, mechanical, and transport processes on wellbore leakage from geologic CO_2 storage reservoirs. Acc. Chem. Res. 50, 1829–1837.

Das, S., Hendry, M., Essilfie-Dughan, J., 2011. Transformation of two-line ferrihydrite to goethite and hematite as a function of pH and temperature. Environ. Sci. Technol. 45, 268–275.

Hewlett, P., 1998. Lea's Chemistry of Cement and Concrete, fourth edition. Arnold, London.

Ian Childers, M., Nguyen, M., Rod, K., Koech, P., Um, W., Chun, J., Glezakou, V., Linn, D., Roosendaal, T., Wietsma, T., Huerta, N., Kutchko, B., Fernandez, C., 2017. Polymer-cement composites with self-healing ability for geothermal and fossil energy applications. Chem. Mater. 29, 4708–4718.

Jacquemet, N., Pironon, J., Saint-Marc, J., 2008. Mineralogical changes of a well cement in various H_2S-CO_2(-brine) fluids at high pressure and temperature. Environ. Sci. Technol. 42, 282–288.

Jung, H., Kabilan, S., Carson, J., Kuprat, A., Um, W., Martin, P., Dahl, M., Kafentzis, T., Varga, T., Stephens, S., Arey, B., Carroll, K., Bonneville, A., Fernandez, C., 2014. Wellbore cement fracture evolution at the cement–Basalt caprock interface during geologic carbon sequestration. Appl. Geochem. 47, 1–16.

Jupe, A., Wilkinson, A., Luke, K., Funkhouser, G., 2008. Class H cement hydration at 180 °C and high pressure in the presence of added silica. Cem. Concr. Res. 38, 660–666.

Koech, P.K., Fernandez, C.A., Rod, K.A., Dai, G., Huerta, N.J., Burton, S., Miller, Q.R.S.,

Resch, C.T., 2020. Advanced self-healing polymer-cement composites for geothermal wellbore applications up to 300 °C. In: PROCEEDINGS World Geothermal Congress. Reykjavik, Iceland.

Kutchko, B., Strazisar, B., Dzombak, D., Lowry, G., Thaulow, N., 2007. Degradation of well cement by CO_2 under geologic sequestration conditions. Environ. Sci. Technol. 41, 4787–4792.

Kutchko, B., Strazisar, B., Lowry, G., Dzombak, D., Thaulow, N., 2008. Rate of CO_2 attack on hydrated class H well cement under geologic sequestration conditions. Environ. Sci. Technol. 42, 6237–6242.

Kutchko, B., Strazisar, B., Huerta, N., Lowry, G., Dzombak, D., Thaulow, N., 2009a. Environ. Sci. Technol. 43, 3947–3952.

Kutchko, B., Strazisar, B., Huerta, N., Lowry, G., Dzombak, D., Thaulow, N., 2009b. CO_2 reaction with hydrated class H well cement under geologic sequestration conditions: effects of flyash admixtures. Environ. Sci. Technol. 43, 3947–3952.

Kutchko, B., Strazisar, B., Hawthorne, S., Lopano, C., Miller, D., Hakala, J., Guthrie, G., 2011. H_2S-CO_2 reaction with hydrated Class H well cement: acid-gas injection and CO_2 co-sequestration. Int. J. Greenh. Gas Control. 5, 880–888.

Kutchko, B., Lopano, C., Strazisar, B., Hawthorne, S., Miller, D., Thaulow, N., Zhang, L., Guthrie, G., 2015. Impact of oil well cement exposed to H_2S saturated fluid and gas at high temperatures and pressures: implications for acid gas injection and Co-sequestration. J. Sustain. Energy Eng. 3, 80–101.

Liu, K., Deng, M., Mo, L., 2015. Influence of pH on the formation of gypsum in cement materials during sulfate attack. Adv. Cem. Res. 27, 487–493.

Lucas, Y., Ngo, V.V., Clément, Al., Fritz, B., Schäfer, G., 2020. Modelling acid stimulation in the enhanced geothermal system of Soultzsous-Forêts (Alsace, France). Geothermics 85, 101772.

Malate, R.C.M., Austria, J.J.C., Sarmiento, Z.F., Di Lullo, G., Sookprasong, P.A., Francis, E.S., 1998. PROCEEDINGS. Twenty-Third Workshop on Geothermal Reservoir Engineering. Stanford University, Stanford, California January 2628, SGP-TR-I58.

Milestone, N.B., Bigley, C.H., Durant, A.T., Sharp, M.D.W., 2010. Effects of CO_2 on Geothermal Cements GRC Transactions 36. pp. 301–306.

Nelson, E., Guillot, D., Cementing, Well, 2006. Schlumberger: Sugar Land, 2nd ed. TX.

Nguyen, M., Wang, Z., Rod, K., Ian Childers, M., Fernandez, C., Koech, P., Bennett, W., Rousseau, R., Glezakou, V., 2018. Atomic origins of the self-healing function in cement–Polymer composites. ACS Appl. Mater. Interfaces 10 (3), 3011–3019.

Paulillo, A., Striolo, A., Lettieri, P., 2019. The environmental impacts and the carbon intensity of geothermal energy: a case study on the Hellisheiði plant. Environ. Int. 133, 105226.

Rickard, D., Luther, G., 1997. Kinetics of pyrite formation by the H_2S oxidation of iron(II) monosulfide in aqueous solutions between 25 and 125 °C: the mechanism. Geochim. Cosmochim. Acta 61, 135–147.

Rod, Kenton, Fernandez, Carlos A., et al., 2020a. Self-repairing polymer-modified cements for high temperature geothermal and fossil energy applications. Geothermics 85, 101790.

Rod, Kenton, Fernandez, Carlos A., et al., 2020b. Polymer-cement composites with adhesion and re-adhesion (healing) to casing capability for geothermal wellbore applications. Cem. Concr. Compos. 107, 103490.

Romanov, V., Soong, Y., Carney, C., Rush, G., Nielsen, B., O'Connor, W., 2015. Mineralization of carbon dioxide: a literature review. ChemBioEng Rev 2, 231–256.

Schoonen, M., Barnes, H., 1991. Reactions forming pyrite and marcasite from solution: I. Nucleation of FeS_2 below 100 °C. Geochim. Cosmochim. Acta 55, 1495–1504.

Shortall, R., Davidsdottir, B., Axelsson, G., 2015. Geothermal energy for sustainable development: a review of sustainability impacts and assessment frameworks. Renew. Sustain. Energy Rev. 44, 391–406.

Thaulow, N., Jakobsen, U., 1997. Deterioration of concrete diagnosed by optical microscopy. Euro seminar on microscopy applied to building materials. In: Proceedings of a Symposium Held in Reykjavik. Iceland. pp. 282–296.

Um, W., Jung, H., Kabilan, S., Fernandez, C., Brown, C., 2014a. Geochemical and geomechanical effects on wellbore cement fractures. Energy Procedia 63, 5808–5812.

Um, W., Jung, H., Kabilan, S., Suh, D., Fernandez, C., 2014b. Geochemical and Geomechanical Effects on Wellbore Cement Fractures: Data Information for Wellbore Reduced Order Model. Pacific Northwest National Laboratory/U.S. Department of Energy, Washington, DC.

Yee, N., Shaw, S., Benning, L., Nguyen, T., 2006. The rate of ferrihydrite transformation to goethite via the Fe(II) pathway. Am. Mineral. 91, 92–96.

Zhang, M., Bachu, S., 2011. Review of integrity of existing wells in relation to CO_2 geological storage: What do we know? Int. J. Greenh. Gas Control. 5, 826–840.

Zhanga, L., Dzombaka, D., Naklesa, D., Hawthorneb, S., Millerb, D., Kutchko, B., Lopanoc, C., Strazisar, B., 2014. Rate of H_2S and CO_2 attack on pozzolan-amended Class H well cement under geologic sequestration conditions. Int. J. Greenh. Gas Control. 27, 299–308.